RSC Advances

PAPER

View Article Online
View Journal | View Issue

Cite this: *RSC Adv.*, 2021, **11**, 26432

First-principles study on structural, electronic and optical properties of perovskite solid solutions $KB_{1-x}Mg_xI_3$ (B = Ge, Sn) toward water splitting photocatalysis†

Chol-Hyok Ri,*[a] Yun-Sim Kim,[a] Un-Gi Jong,[a] Yun-Hyok Kye,[a] Se-Hun Ryang[b] and Chol-Jun Yu[a]

Perovskite materials have been recently attracting a great amount of attention as new potential photocatalysts for water splitting hydrogen evolution. Here, we propose lead-free potassium iodide perovskite solid solutions KBI_3 with B-site mixing between Ge/Sn and Mg as potential candidates for photocatalysts based on systematic first-principles calculations. Our calculations demonstrate that these solid solutions, with proper Goldschmidt and octahedral factors for the perovskite structure, become stable by configurational entropy at finite temperature and follow Vegard's law in terms of lattice constant, bond length and elastic constants. We calculate their band gaps with different levels of theory with and without spin–orbit coupling, revealing that the hybrid HSE06 method yields band gaps increasing along the quadratic function of Mg content x. Moreover, we show that the solid solutions with $0.25 \leq x \leq 0.5$ have appropriate band gaps between 1.5 and 2.2 eV, reasonable effective masses of charge carriers, and suitable photoabsorption coefficients for absorbing sunlight. Among the solid solutions, $KB_{0.5}Mg_{0.5}I_3$ (B = Ge, Sn) is found to have the most promising band edge alignment with respect to the water redox potentials with different pH values, motivating experimentalists to synthesize them.

Received 11th June 2021
Accepted 2nd July 2021

DOI: 10.1039/d1ra04534b

rsc.li/rsc-advances

1. Introduction

Photocatalytic water splitting is an attractive method for solar hydrogen production toward a sustainable and clean energy economy.[1–8] In fact, hydrogen combustion generates a significant amount of heat without release of any pollutant, being converted into pure water. Among various hydrogen production methods, such as steam methane reforming, coal or biomass gasification and electrolysis, solar water splitting is the most promising for energy production in the sense of energy balance. The key issue in progressing this technology for commercially viable large-scale utilization is to develop photocatalysts with high conversion efficiency, long-term durability, affordable cost and sufficient reserve. In this line, there are plenty of photocatalysts including carbon nitride Z-scheme systems,[9] mesoporous g-C_3N_4 nanosheets,[10] g-C_3N_4-based nanocomposites,[11] Ag-based nanocomposites,[12] TiO_2,[13] Ir-based photosensitizers[14,15] and orchestrated photosensitizers.[16] Metal halide perovskites with the chemical formula ABX_3 (A: organic or inorganic monovalent cation, B: divalent metal cation, X: halide anion) have aroused an increasing interest in photocatalytic[17–21] as well as photovoltaic applications.[22–25] With the ease of preparation and low cost of fabrication, the power conversion efficiency of perovskite solar cells (PSCs) has rapidly evolved from the initial value of 3.8% in 2009 (ref. 25) to the latest certified record of 25.5% in 2020.[26] Moreover, there is a great diversity of compositional change in ABX_3, making it easy to tune their band gap and optoelectronic properties.[27–29]

To provoke solar water splitting, the electronic band structure of a photocatalyst is required to be properly matched with the reaction redox potential. Moreover, considering the solar spectrum with ultraviolet (UV) range of ~3% and visible range of ~45%, the band gap should be placed in the proper value range for visible light absorption. This can be achieved by tailoring an appropriate composition in ABX_3 perovskites with suitable positions of the conduction band (CB) for hydrogen evolution reaction (HER) and/or the valence band (VB) for oxygen evolution reaction (OER).[19] Photocatalytic H_2 generation

[a]Chair of Computational Materials Design (CMD), Faculty of Materials Science, Kim Il Sung University, Ryongnam-Dong, Taesong District, Pyongyang, Democratic People's Republic of Korea. E-mail: cj.yu@ryongnamsan.edu.kp

[b]Chair of Theoretical Physics, Faculty of Physics, Kim Hyong Jik University of Education, Ryul-Dong, Dongdaewon District, Pyongyang, Democratic People's Republic of Korea

† Electronic supplementary information (ESI) available: Computational details of elastic constants and modulus, tables for lattice constants and band gaps of $CsBI_3$ (B = Mg, Ge, Sn), elastic constants and modulus, band gaps of solid solutions, and figures for crystalline structures, linear relation between volume and density, partial density of states, fitting lines of band gaps with HSE06, phonon dispersion curves, and real and imaginary parts of frequency-dependent dielectric constants. See DOI: 10.1039/d1ra04534b

was first observed in hybrid organic–inorganic methylammonium lead iodide $MAPbI_3$ with an optimal band gap of 1.5–1.6 eV, being dissolved in saturated HI acid aqueous solution.[30] Significant enhancement of H_2 generation was reported for some $MAPbI_3$ composites with, for example, Pt, Pt/TiO_2,[31,32] reduced graphene oxide,[33] and black phosphorus.[34] With a broader band gap of ~2.3 eV, $MAPbBr_3$ bulk microcrystals in saturated HBr solution were also shown to improve photocatalytic H_2 production upon visible light irradiation.[35] However, the organic–inorganic hybrid perovskites have severe problems of structural and chemical degradation upon exposure to sunlight, heat and moisture.[36–38]

The all-inorganic perovskites, which can be formed by replacing the A site organic cation with inorganic Cs^+ or Rb^+, have been proved to increase resistance to humidity with improving photostability.[39–41] The cesium lead halide perovskites $CsPbX_3$ (X = Br, I) are promising photocatalysts for H_2 production in the form of quantum dots (QDs) with a good structural stability under the reaction conditions.[42,43] When mixing iodide and bromide to form $CsPbBr_{3-x}I_x$ with a band gap funnel structure,[44,45] the $CsPbBr_{3-x}I_x$/Pt photocatalyst has a high stability with HER capability in a saturated HBr/HI mixed solution.[45] To avoid the toxicity problem from lead,[46] remarkable research endeavors were devoted to developing lead-free halide perovskites.[47–52] The most primary elements for lead substitution are Sn and Ge due to their electronic configurations being similar to Pb, however, with relatively low chemical stability and low efficiency.[53,54] The alkaline-earth elements such as Mg, Ca and Sr with a stable +2 oxidation state are also not excluded on the condition that the Goldschmidt tolerance factor[55] is satisfied for the stable perovskite structure (t, $0.8 < t < 1.0$).[50–52] On the other hand, the potassium element (K) can be a potential candidate for Cs^+, Rb^+ and MA cation in the A site, considering that it can be matched with Ge and Sn in the B site for the tolerance factor.[56–58] Based on such considerations, it could be foreseen that $KGeI_3$, $KSnI_3$ and $KMgI_3$ are possible to be formed in a perovskite structure. Moreover, these compounds are composed of low cost, earth abundant and environment friendly elements, being potential candidates for replacing toxic and relatively high cost $MAPbI_3$ and $CsPbI_3$ or $RbPbI_3$.

In this work, we systematically investigate the structural, mechanical, electronic, and optical properties of potassium iodide B-site cation mixing solid solutions $KB_{1-x}Mg_xI_3$ (B = Ge, Sn) in tetragonal phase using density functional theory (DFT) calculations. Especially, as it is important to assess the absolute energy level (band edge) alignment of a system in searching the potential candidates for photocatalysis, we calculate energy levels relative to the hydrogen reduction level with band gaps on the basis of inspecting the reliability and accurateness of our calculation approach.

2. Computational methods

Most calculations were performed using the ultrasoft pseudopotential plane-wave method as implemented in VASP.[59] Ultrasoft pseudopotentials were used for all the atoms with the valence electron configurations of K-$3s^23p^64s^1$, Ge-$4s^24p^2$, Sn-$5s^25p^2$, Mg-$3s^23p^0$ and I-$5s^25p^5$. The crystalline structures of B-site cation solid solutions $KB_{1-x}Mg_xI_3$ (B = Ge, Sn) were modeled with a tetragonal unit cell containing 4 formula units, and the symmetric slab models with 13 atomic layers and a vacuum region of 15 Å are used for the (001) surface. We used a kinetic cutoff energy of 500 eV for a plane-wave basis set. To perform the Brillouin-zone (BZ) integration for calculating electron density, we adopted Γ-centered k-point meshes of ($6 \times 6 \times 4$) for structural optimization of bulk and ($6 \times 6 \times 1$) for surface relaxation. These computational parameters guarantee the total energy convergence as 5 meV per formula unit. The atomic positions were relaxed until the forces on atoms converged to 0.01 eV $Å^{-1}$ while keeping the middle 5 atomic layers fixed to the bulk positions.

The exchange–correlation interaction between the valence electrons was described by the Perdew–Burke–Ernzerhof (PBE) formalism[60] within the generalized gradient approximation (GGA) for all geometry optimizations. To get more reliable band gaps and absolute band energy levels, we also used the Heyd–Scuseria–Ernzerhof (HSE) hybrid functional[61,62] with a 25% portion of the exact exchange functional. The spin–orbital coupling (SOC) effect was considered only for the electronic band structure calculations. We adopted a lower plane-wave cutoff energy of 40 Ry and smaller k-point grids of $3 \times 3 \times 2$ and $3 \times 3 \times 1$ for the bulk and surface models with HSE06 and HSE06+SOC methods.

The B-site cation exchange effects were tested using the tetragonal $KMgI_3$ unit cell, which has four different B-cation sites. Therefore, we considered five different compositions of Mg and B (B = Ge and Sn) in $KB_{1-x}Mg_xI_3$ as $x = 0$, 0.25, 0.5, 0.75 and 1, as shown in Fig. 1. To check the thermodynamic miscibility of solid solutions, we computed the Helmholtz free energy difference for each composition as

$$\Delta F = \Delta U - T\Delta S \quad (1)$$

where ΔU and ΔS are the internal energy and entropy difference and T is the temperature. Here, the internal energy difference was calculated using

$$\Delta U = E_{KB_{1-x}Mg_xI_3} - (1-x)E_{KBI_3} - xE_{KMgI_3} \quad (2)$$

where $E_{KB_{1-x}Mg_xI_3}$, E_{KBI_3}, E_{KMgI_3} (B = Ge, Sn) are the total energies of corresponding compounds. The entropy difference was evaluated in the homogeneous limit using

$$\Delta S = -k_B[(1-x)\ln(1-x) + x\ln x] \quad (3)$$

where k_B is the Boltzmann constant. A similar approach has been applied to study the thermodynamic stability of halide perovskite solid solutions.[39,49,63]

To assess the mechanical stability of crystalline solids, we calculated the elastic stiffness (C_{ij}) and compliance (S_{ij}) constants. For the tetragonal structure, there are six independent elastic constants: $ij = 11$, 12, 13, 33, 44 and 66. The bulk (B) and shear (G) moduli are calculated within different approximations such as Voigt, Reuss and Hill (see ESI† for details), as

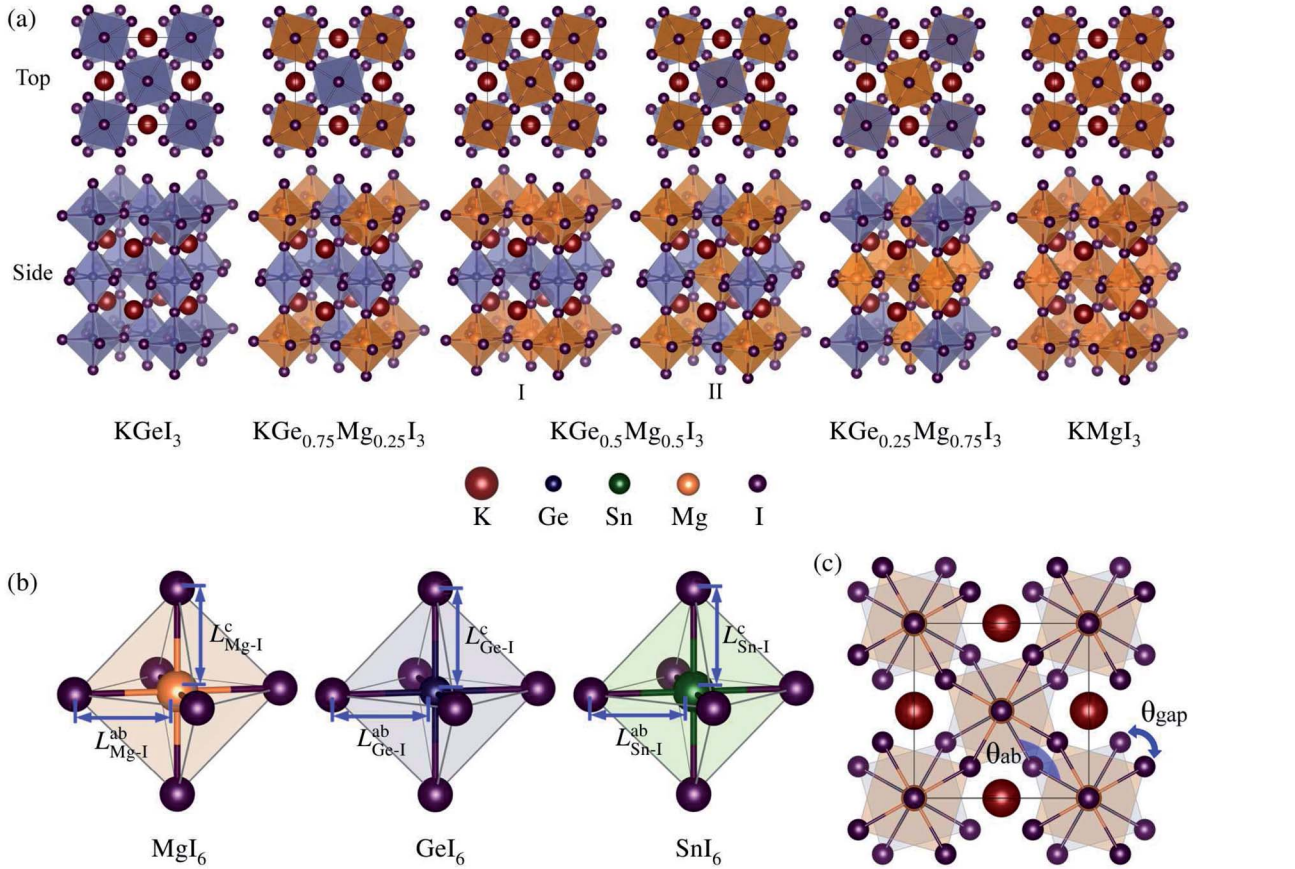

Fig. 1 (a) Polyhedral view of unit cells of potassium iodide B-site mixed perovskite solid solutions $KGe_{1-x}Mg_xI_3$ in tetragonal phase with $x = 0$, 0.25, 0.5 (I, II), 0.75 and 1. (b) Bond length L^{ab}_{B-I} on the *ab* plane and L^{c}_{B-I} along the *c* axis for B–I bonds within the BI_6 octahedral cage (B = Mg, Ge, Sn). (c) Distortion angle θ_{ab} defined by the B–I–B bond angle within the BI_6 octahedral cages on the *ab* plane, and gap angle θ_{gap} defined by the angle between the upper and lower BI_6 cages.

we have already applied to other tetragonal crystals.[64] We also calculated the Young's modulus (E) and Poisson's ratio (ν) from the calculated bulk and shear moduli. Then, the longitudinal (v_l) and transverse (v_t) elastic wave velocities, the average sound velocity (v_{av}), and Debye temperature (θ_D) were determined.

The macroscopic frequency-dependent dielectric functions, $\varepsilon(\omega) = \varepsilon_1(\omega) + i\varepsilon_2(\omega)$ with the frequency of light ω, were calculated by solving the Bethe–Salpeter equation within random phase approximation (RPA), neglecting the local field effect (LFE),[65] using the ABINIT package (version 8.4.4).[66] We adopted the Gaussian smearing with a broadening parameter of 0.13 eV for the interband contribution. We then determine the photoabsorption coefficients as a function of frequency, $\alpha(\omega)$, as follows

$$\alpha(\omega) = \frac{\sqrt{2}\omega}{c}\sqrt{\sqrt{\varepsilon_1{}^2(\omega) + \varepsilon_2{}^2(\omega)} - \varepsilon_1(\omega)} \quad (4)$$

where c is the light velocity in vacuum. We note that a similar method has been successfully applied to the perovskite materials.[44,67,68]

Given the electronic band structures $E(\boldsymbol{k})$ as a function of wavevector $\boldsymbol{k}$, we estimate the effective masses of electron and hole by numerically performing the second derivative of energy *versus* wave vector at the valence band maximum (VBM) and conduction band minimum (CBM) as

$$\frac{1}{m^*_h} = \frac{1}{\hbar^2}\frac{\partial^2 E_{VBM}(\boldsymbol{k})}{\partial \boldsymbol{k}^2}, \quad \frac{1}{m^*_e} = \frac{1}{\hbar^2}\frac{\partial^2 E_{CBM}(\boldsymbol{k})}{\partial \boldsymbol{k}^2} \quad (5)$$

where $\hbar$ is the reduced Planck's constant. In design of photocatalysts, it is important to accurately determine the absolute VBM and CBM energy levels (E_{VBM}, E_{CBM}) with respect to an external vacuum level. As suggested in previous works,[49,69] we compute the electrostatic potential of the (001) surface after relaxation and fix the obtained external vacuum level as a reference level. Through core level calculations with the bulk and surface unit cells, we choose the K 1s level as the representative core level, and estimate the absolute energy levels E_{VBM} and E_{CBM} of the bulk phases using

$$E_{VBM} = \varepsilon^{KS}_{VBM} - (E^{bulk}_{K1s} - E^{surf}_{K1s}) - V_{vac} \quad (6)$$

$$E_{CBM} = \varepsilon^{KS}_{CBM} - (E^{bulk}_{K1s} - E^{surf}_{K1s}) - V_{vac} \quad (7)$$

where ε^{KS}_{band} is the Kohn–Sham (KS) eigenvalue in the bulk phase corresponding to the band, E^{bulk}_{K1s} and E^{surf}_{K1s} are the average K 1s levels in the bulk phase and in the innermost seven layers of the

surface slab model, and V_{vac} is the vacuum level obtained from the planar average electrostatic potential.

3. Results and discussion

3.1 Structural and mechanical stability

Halide materials with a chemical formula ABX_3 can be formed in different crystal structures depending on the size of ions and interaction between the A cation and BX_6 octahedra. Goldschmidt tolerance factor (t_G) is a useful index to predict which crystal structure is favorable.[70] Using the ionic radii r, the Goldschmidt tolerance factor of KBI_3 (B = Mg, Ge, Sn) is calculated as follows,[55,71]

$$t_G = \frac{r_K + r_I}{\sqrt{2}(r_B + r_I)} \quad (8)$$

With the established ionic radii of $r_K = 1.38$ Å, $r_{Mg} = 0.72$ Å, $r_{Ge} = 0.73$ Å, $r_{Sn} = 1.18$ Å and $r_I = 2.16$ Å,[72] the t_G values are obtained as 0.869, 0.866, and 0.749 for B = Mg, Ge, and Sn, respectively. According to the previous reports,[55,73] a cubic perovskite structure can be formed when $0.9 \leq t_G \leq 1.0$, while as decreasing t_G from 0.9 to 0.8 tetragonal, orthorhombic and rhombohedral perovskite structures can be favorable. Otherwise, a non-perovskite structure is formed when $t_G > 1$ or $t_G < 0.8$. For the cases of B = Mg and Ge, these B-site cations can surely form perovskite structures with A-site K^+ cation and I^- anion due to their t_G values being within the safe range of [0.8, 1]. Meanwhile, the calculated t_G value for B = Sn is 0.749, being smaller than the safe value of 0.8, but mixing with Mg increases t_G values over 0.8 from $x = 0.5$. Since the t_G values are lower than 0.9, we adopt the tetragonal KBI_3 with space group of *P4/mbm* in the following study. Table 1 lists the t_G values for B-site cation mixing iodide solid solutions $KB_{1-x}Mg_xI_3$ (B = Ge, Sn) as well, calculated using the average ionic radius of the $B_{1-x}Mg_x$ ion. It is rightly found that $0.866 \leq t_G \leq 0.869$ for $KGe_{1-x}Mg_xI_3$ solid solutions and $0.749 \leq t_G \leq 0.869$ for $KSn_{1-x}Mg_xI_3$.

In the halide perovskite structure, the large monovalent A-site cation forms an AX_{12} cuboctahedron with the nearest 12 X anions, whereas the smaller divalent B-site cation is bonded with the nearest 6 X anions forming corner-sharing BX_6 octahedra. The stability of the BX_6 octahedron is measured by the octahedral factor $\mu = r_B/r_X$, which should be within the range of $0.44 \leq \mu \leq 0.9$ for a stable perovskite.[74] On the other hand, Travis *et al.* reported $\mu \geq 0.41$ as a limit octahedral factor for the ABI_3 perovskite structure.[55] For the cases of B = Mg, Ge and Sn, the μ values are calculated as 0.333, 0.338 and 0.546, respectively. This indicates that among the three compounds $KSnI_3$ has the most stable octahedra, while $KGeI_3$ and $KMgI_3$ are less favorable for octahedral stability. However, their μ values are comparable with 0.338 of $CsGeI_3$, which was experimentally found to form a stable perovskite structure.[48,54] When mixing the B-site Mg^{2+} cation with Ge or Sn, the obtained solid solutions have improving octahedral stability with their increasing μ values, which are 0.333–0.338 for $KGe_{1-x}Mg_xI_3$ and 0.333–0.546 for $KSn_{1-x}Mg_xI_3$.

Optimized structures of $KGe_{1-x}Mg_xI_3$ solid solutions with $x = 0.0$, 0.25, 0.5, 0.75 and 1.0 are shown in Fig. 1(a). Similar structures are also observed for $KSn_{1-x}Mg_xI_3$ solid solutions (Fig. S1†). With the tetragonal unit cell, one unique structure is possible for $x = 0.25$ and 0.75, but two distinct structures can be considered for $x = 0.5$ solid solutions by way of mixing B-site cations: I and II with the same and different elements on the (001) plane (see Fig. S2† for linear relation between volume and density).

We calculate the elementary formation energy $E_f = E_{KBI_3} - (E_K^{fcc} + E_B^{bulk} + E_I^{orth})$ using the total energies of bulk unit cells of the elements. Face-centered cubic (fcc) phase for K and Ge, body-centered cubic (bcc) phase for Sn, hexagonal phase for Mg and orthorhombic phase for I elementary bulks are adopted. In addition, the cohesive energy is calculated as $E_c = E_{KBI_3} - (E_K^{atom} + E_B^{atom} + E_I^{atom})$ using the total energies of the isolated atoms. Table 1 lists the calculated values, all of which are found to be negative, indicating their certain formability from the constituent elementary bulks.

To systematically investigate the effect of B-site cation mixing on the bulk properties of these solid solutions, we plot their lattice constants and Helmholtz free energy of mixing as a function of B/Mg ratio x (B = Ge, Sn) in Fig. 2. Here, all markers indicate the calculated values, and dashed lines in Fig. 2(a) and (b) show linear fitting results, *i.e.*, Vegard's law, where KBI_3 (B = Ge, Sn) and $KMgI_3$ are set as two end compounds. Our optimized lattice constants a and c are shown to decrease with increasing the Mg fraction x in both kinds of solid solutions, which might be due to the smaller ionic radius of Mg (0.72 Å) than Ge (0.73 Å) and Sn (0.93 Å). The decreasing tendency is more pronounced for B = Sn solid solutions, while c is scarcely changed with x in $KGe_{1-x}Mg_xI_3$. This is also associated with the comparable ionic radii of Mg and Ge, affecting the miscibility discussed below. Linear functions with decreasing tendency are obtained as $a(x) = 8.583 - 0.550x$ (Å) with a correlation coefficient of 0.999 and $c(x) = 12.556 - 0.563x$ (Å) with 0.998 correlation coefficient for $KSn_{1-x}Mg_xI_3$ with $x = 0.5$ (I). For $KGe_{1-x}Mg_xI_3$, they are $a(x) = 8.231 - 0.215x$ (Å) with a reasonably high correlation coefficient of 0.991 and $c(x) = 12.050 - 0.019x$ (Å) with a remarkably low correlation

Table 1 Goldschmidt tolerance factor (t_G), octahedral factor (μ), elementary formation energy per atom (E_f) and cohesive energy per atom (E_c) in potassium iodide B-site mixed solid solutions $KB_{1-x}Mg_xI_3$ (B = Ge, Sn)

System	x	t_G	μ	E_f (eV)	E_c (eV)
$KGe_{1-x}Mg_xI_3$	0.00	0.866	0.338	−25.22	−2.69
	0.25	0.867	0.337	−19.35	−2.64
	0.50 (I)	0.868	0.336	−13.53	−2.60
	0.50 (II)	0.868	0.336	−13.48	−2.60
	0.75	0.868	0.334	−7.72	−2.56
	1.00	0.869	0.333	−1.97	−2.52
$KSn_{1-x}Mg_xI_3$	0.00	0.749	0.546	−16.07	−2.67
	0.25	0.776	0.493	−12.43	−2.63
	0.50 (I)	0.805	0.440	−8.70	−2.59
	0.50 (II)	0.805	0.440	−8.85	−2.60
	0.75	0.836	0.387	−5.18	−2.56
	1.00	0.869	0.333	−1.66	−2.52

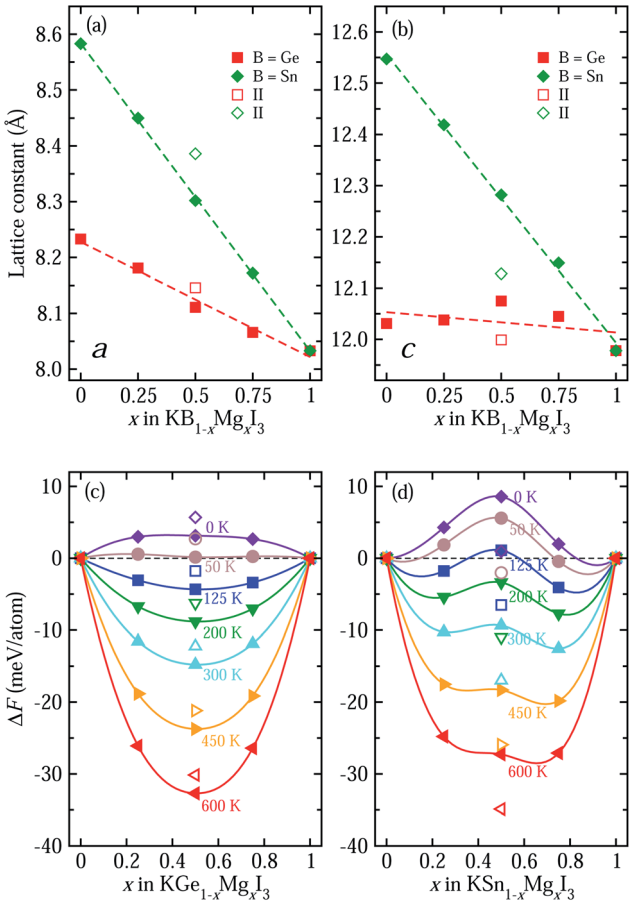

Fig. 2 (a) Lattice constants *a* and (b) *c* of potassium iodide perovskite solid solutions $KB_{1-x}Mg_xI_3$ (B = Ge, Sn) in tetragonal phase as a function of Mg content *x*. Dashed lines are drawn by linear fitting. (c) Helmholtz free energy of mixing in B = Ge and (d) B = Sn solid solutions at various temperatures, using two end compounds of $KGeI_3$/$KSnI_3$ and $KMgI_3$.

coefficient of 0.219. Noticeable deviation from linear function is found for $x = 0.5$ (II) compounds.

The constituent atoms can be slightly displaced at finite temperature, leading to tilting or distortion of BI_6 octahedra. To quantify the degree of such octahedral tilting or distortion, we measure the bond length L^{ab}_{B-I} on the *ab* plane and L^{c}_{B-I} along the *c* axis for the B–I bond within the BI_6 octahedral cage (B = Mg, Ge, Sn), as depicted in Fig. 1(b). The measured bond lengths are listed in Table 2. It is found that $L^{ab}_{B-I} < L^{c}_{B-I}$ for B = Mg and Ge, whereas $L^{ab}_{B-I} > L^{c}_{B-I}$ for B = Sn, indicating a clear octahedral distortion. The magnitude of the bond length is in the order of Mg < Ge < Sn as is the order of ionic radius. We also define the distortion angle θ_{ab} by the B–I–B bond angle within the BI_6 octahedral cages on the *ab* plane, and the gap angle θ_{gap} by the angle between upper and lower BI_6 cages, as shown in Fig. 1(c). Obviously, $\theta_{ab} = 180°$ and $\theta_{gap} = 0°$ are satisfied for an ideal cubic perovskite, and $\theta_{ab} + \theta_{gap} = 180°$ for the ideal tetragonal phase. For B = Mg, Ge, and Sn, the average values of θ_{ab} are 28.70°, 28.89° and 33.75°, whereas those of θ_{gap} are 151.30°, 151.10° and 146.25°, with the sum of almost 180° (Table 2). When mixing the B-site cations, the resultant solid solutions show some deviation from the ideal tetragonal phase.

To assess the miscibility of solid solutions, we calculate the Helmholtz free energy of mixing according to eqn (1)–(3) as a function of Mg content *x* in $KB_{1-x}Mg_xI_3$ with increasing temperature, as shown in Fig. 2(c) and (d). At 0 K, the entropy effect plays no role in the free energy and only the internal (DFT) energy difference is considered. Thus, all values are calculated to be positive for both kinds of solid solutions, implying that the solid solutions are readily separated into the constituent phases of KBI_3 (B = Ge, Sn) and $KMgI_3$. However, the entropy of mixing contributes highly to the free energy at higher temperature, resulting in gradual stabilization of the solid solutions with a negative free energy difference. In fact, the $KGe_{1-x}Mg_xI_3$ solid solution is found to be stabilized at over 50 K, while for the $KSn_{1-x}Mg_xI_3$ solid solution the stabilization temperature is higher at around 125 K. This indicates that Mg is more readily mixed with Ge than with Sn on the B-site in KBI_3 perovskite, which is also associated with the closer ionic radius of Mg to that of Ge. When compared with other perovskite solid solutions, their critical temperatures of 50 and 125 K are lower than 140 K for tin-based A-site solid solution $Rb_xCs_{1-x}SnI_3$ (ref. 49) and 343 K for halide anion mixing $MAPb(I_{1-x}Br_x)_3$.[63] The phonon dispersions of solid solutions with typically $x = 0.5$ were calculated to assess the dynamical stability, revealing the imaginary phonon modes and thus indicating the phase transition with varying temperature (Fig. S5†).

We then consider the mechanical stability of perovskite solid solutions by calculating elastic constants and the connected quantities. Fig. 3(a)–(c) show the calculated elastic stiffness constants of perovskites in the tetragonal phase, which has six independent components of C_{11}, C_{12}, C_{13}, C_{33}, C_{44} and C_{66} (Table S3†). Firstly, it is found that the calculated elastic constants meet the Born requirements for mechanical stability of tetragonal crystals: $C_{11} > 0$, $C_{33} > 0$, $C_{44} > 0$, $C_{66} > 0$, $C_{11} - C_{12} > 0$, $C_{11} + C_{33} - 2C_{13} > 0$, and $2(C_{11} + C_{12}) + C_{33} + 4C_{13} > 0$. This indicates that these perovskites have a strong resistance to mechanical deformation. It is worth noting that C_{33} is larger than C_{11} for all the compounds, indicating that their resistances to deformation along the *c*-axis are stronger than those along the *a*-axis. It is also shown that as the Mg content *x* increases in $KGe_{1-x}Mg_xI_3$ solid solution, C_{11} increases from 262.2 GPa to 279.5 GPa, C_{33} decreases from 431.9 GPa to 345.9 GPa, and C_{44} related to shear deformation resistance decreases from 150.8 GPa to 102.6 GPa. Therefore, the deformation resistance along the *c*-axis and shear deformation resistance can be said to be weakened by substituting Mg with a smaller ionic radius for Ge on the B-site. A similar tendency is observed for Sn-based solid solutions $KSn_{1-x}Mg_xI_3$.

For a polycrystalline solid, the mechanical stability is assessed by elastic modulus, such as bulk modulus (B), shear modulus (G) and Young's modulus (E), which can be directly calculated from the elastic stiffness and compliance constants (Tables S3–S5†). Fig. 3(d) shows the moduli calculated within the Hill approximation as the average between the lower and

Table 2 The average bond lengths on the *ab* plane (L^{ab}_{B-I}) and along the *c* axis (L^{c}_{B-I}) for B–I bonds within the BI_6 octahedral cage (B = Mg, Ge, Sn), depicted in Fig. 1(b), and the distortion angle defined by the B–I–B bond angle on the *ab* plane (θ_{ab}) and the gap angle between upper and lower octahedra (θ_{gap}), shown in Fig. 1(c), in potassium iodide perovskite solid solutions $KGe_{1-x}Mg_xI_3$ and $KSn_{1-x}Mg_xI_3$

		B–I bond length within BI_6 octahedron (Å)						Distortion angle (deg)		
		L^{ab}_{B-I}			L^{c}_{B-I}					
System	*x*	B = Ge	B = Sn	B = Mg	B = Ge	B = Sn	B = Mg	θ_{gap}	θ_{ab}	$\theta_{gap} + \theta_{ab}$
$KGe_{1-x}Mg_xI_3$	0.00	3.009	—	—	3.009	—	—	28.89	151.10	179.99
	0.25	3.007	—	2.947	3.026	—	2.990	29.82	150.39	180.21
	0.50 (I)	2.982	—	2.969	3.033	—	2.969	30.41	149.60	180.01
	0.50 (II)	3.021	—	2.922	3.020	—	3.017	29.04	151.93	180.97
	0.75	3.006	—	2.930	3.020	—	3.009	29.28	149.12	178.40
	1.00	—	—	2.932	—	—	2.995	28.70	151.30	180.00
$KSn_{1-x}Mg_xI_3$	0.00	—	3.171	—	—	3.138	—	33.75	146.25	180.00
	0.25	—	3.165	2.976	—	3.140	2.999	33.82	148.83	182.65
	0.50 (I)	—	3.114	3.004	—	3.175	2.889	32.49	147.51	180.00
	0.50 (II)	—	3.181	2.931	—	3.158	2.983	30.93	153.77	184.70
	0.75	—	3.153	2.946	—	3.147	2.999	30.02	146.11	176.13
	1.00	—	—	2.932	—	—	2.995	28.70	151.30	180.00

upper limits within the Voigt and Reuss approximations, respectively (Table S4†). Interestingly, the change tendencies are found to be different for Ge- and Sn-based solid solutions. For the case of $KGe_{1-x}Mg_xI_3$, with increasing the Mg content *x*, the bulk modulus gradually increases while the shear and Young's moduli decrease. On the contrary, the three kinds of elastic moduli increase with the Mg content *x* in $KSn_{1-x}Mg_xI_3$. It should be noted that bulk, shear and Young's moduli are associated with the mechanical stability to uniform pressure, shear and uniaxial stress, respectively. Moreover, the ductility of solid solutions are tested by estimating Pugh's ratio (*B*/*G*) and Poisson's ratio (ν), as shown in Fig. 3(e) and (f). Considering that a solid with a Pugh's ratio greater than 1.75 and/or Poisson's ratio larger than 0.26 is a ductile material,[75] all solid solutions are found to be ductile due to their *B*/*G* and ν values satisfying the Pugh criteria for ductility. Here, it is worth noting that Ge replacement by Mg enhances the ductility due to the increasing *B*/*G* and ν, but Sn replacement worsens the ductility.

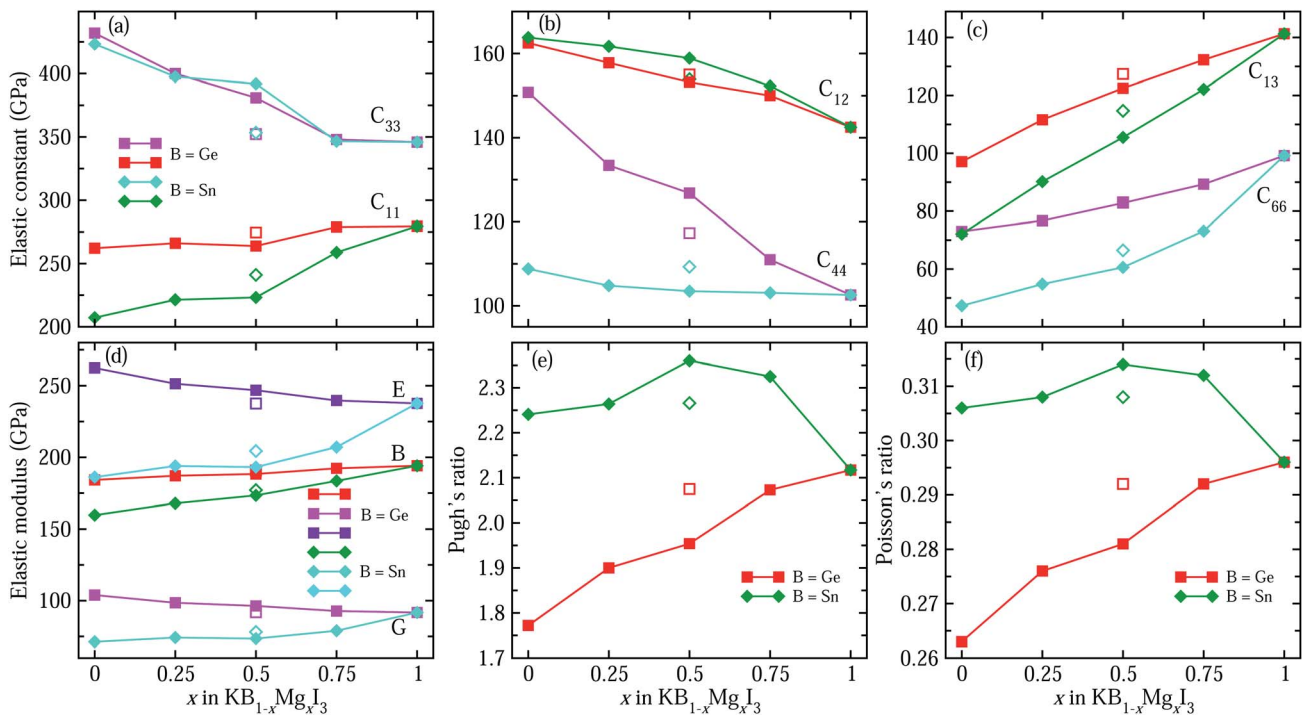

Fig. 3 Six independent elastic constants of (a) C_{11}, C_{33}, (b) C_{12}, C_{44}, (c) C_{13} and C_{66}, (d) elastic modulus including bulk modulus *B*, shear modulus *G* and Young's modulus *E*, (e) Pugh's ratio *B*/*G*, and (f) Poisson's ratio ν as a function of Mg content *x* in potassium iodide perovskite solid solutions $KB_{1-x}Mg_xI_3$ (B = Ge, Sn) in tetragonal phase, calculated with PBE functional.

3.2 Electronic and optical properties

Provided that the potassium iodide perovskite solid solutions $KB_{1-x}Mg_xI_3$ (B = Ge, Sn) are stable to be formed, we calculate their electronic band structures with density of states (DOS). It is known that an error cancellation between the GGA underestimation and SOC ignoring overestimation occurs in the hybrid iodide perovskite $MAPbI_3$ and thus PBE yields its band gap in good agreement with experiment.[76] However, PBE underestimates band gaps for all-inorganic Ge-based ($CsGeX_3$)[69] and Sn-based perovskites ($CsSnI_3$).[49] Including the SOC effect leads to splitting and lowering of CBM, resulting in further underestimation of band gap.[76] Reasonable band gaps for $CsGeX_3$ agreeing well with experiment were obtained by applying the hybrid functional HSE06, while HSE06+SOC yielded underestimated values.[69] In this work, therefore, we use different levels of DFT methods, PBE and HSE06 with and without SOC effect, to obtain reasonable band gaps.

Fig. 4 shows the electronic band structures with partial density of states (DOS) calculated with PBE and band gaps obtained by using PBE and HSE06 functionals with and without SOC as a function of Mg content x in $KB_{1-x}Mg_xI_3$ (B = Ge, Sn) (see Table S5† for band gaps). We note that the band structures and DOS obtained with HSE06 are almost identical in shape with those using PBE, and the positions are only shifted upward and downward.[69] For $KGeI_3$ and $KSnI_3$, the VBM states are found to be mainly contributed by I 5p with a small amount of Ge/Sn 4s/5s states, while the CBM states are dominated by Ge/Sn 4p/5p states in weak hybridization with I 5p states. For the case of $KMgI_3$, the VBM state is dominated by I 5p states and the CBM state is composed of strong hybridization between Mg 3s and I 5p states (Fig. S3†). Potassium (K) atoms hardly contribute to the CBM and VBM states. The spherical shape and distribution of VBM and CBM states in KBI_3 (B = Mg, Ge, Sn) are clearly shown in Fig. 5. We also discuss the band dispersion, which is important for assessing the mobility of charge carriers. For $KGeI_3$ and $KSnI_3$, the valence and conduction bands are found to be dispersive, implying small effective masses of hole and electron. However, the valence band of $KMgI_3$ looks quite flat, indicating a large effective mass of hole and thus its low mobility, although the conduction band is highly dispersive. This band dispersion feature of the Mg-based perovskite reflects the flat valence bands of $B_{1-x}Mg_x$-based solid solutions, in particular high Mg contents of $x = 0.75$ and 0.5 for both B = Ge and Sn. It is worth noting that the folded and entangled bands can be originated from using the unit cell with 4 formular units, affecting the nature of the band gap (direct or indirect), and thus unfolding the bands structures back to the Brillouin zone of a hypothetical smaller cell can be considered.

For $KGeI_3$, the band gaps are calculated to be 0.85/0.62 eV with PBE/PBE+SOC and 1.24/1.04 eV with HSE06/HSE06+SOC (Table S6†). When compared with the previous calculation, HSE06+SOC among the methods yields the closest value to 1.08 eV with GLLB-SC (meta-GGA functional by Gritsenko, van Leeuwen, van Lenthe, and Baerends with PBEsol correlation for solid).[72] Also, among the band gaps of $KSnI_3$, 0.66/0.59 eV and 1.07/1.02 eV calculated with PBE/PBE+SOC and HSE06/HSE06+SOC methods, HSE06+SOC gives the best agreement with the GLLB-SC calculation of 0.97 eV.[72] It is worth noting that the inclusion of SOC underestimates band gaps of semiconductors due to lowering the CBM but its effect is much weaker for the lighter elements of Sn and Ge than for Pb. In fact, the differences in band gaps between inclusion and no inclusion of SOC with PBE and HSE06 were estimated to be 0.20 and 0.24 eV for $KGeI_3$, 0.12 and 0.09 eV for $KMgI_3$, and 0.05 and 0.06 eV for $KSnI_3$, respectively. It should be noted that for the all-inorganic iodide perovskites the difference between HSEO06 and HSE06+SOC is quite small, in the order of ~0.1 eV, compared with bromides (~0.6 eV) and chlorides (~1.0 eV),[69] and HSE06 was found to give the band gaps in the best agreement with experiment (see Table S2† for our calculations). Therefore, we regard that the band gaps determined by HSE06 are the most reliable although HSE06+SOC gives the closer values to those with GLLB-SC.

According to the B-site cation in the iodide perovskites KBI_3 (B = Mg, Ge, Sn), their band gaps with HSE06 are found to be in the order of Sn (1.07 eV) < Ge (1.24 eV) < Mg (2.92 eV), which are in the reverse order to their ionic radii. This indicates that the small cationic size of the B-site cation in potassium iodide perovskites is responsible for the small size of the BI_6 octahedron and increasing band gap. When mixing Ge/Sn with Mg, the band gap is found to increase with the Mg content x following the quadratic function of $E_g(x) = E_g(0) + [E_g(1) - E_g(0) - b]x + bx^2$ with the bowing parameter b (ref. 40 and 44) (see Table S7 and Fig. S4†). The values of b with $x = 0.5$ (I) are estimated to be smaller than those with $x = 0.5$ (II); −0.76 *vs.* −2.06 and 0.27 *vs.* −1.90 for B = Ge and Sn, respectively. The solid solutions with $0.25 \leq x \leq 0.5$ for Mg content are found to be suitable for absorbing sunlight and photocatalysis with band gaps of 1.5–2.2 eV. Moreover, from the band structures, the solid solutions with $x = 0.25$ are shown to have direct band gaps at the BZ center Γ point, which is beneficial for device efficiency.

We also calculate the effective masses of charge carriers to assess their mobility, as listed in Table 3. As expected from the band dispersion, the effective masses of electrons m_e^* in Ge/Sn-based perovskites (0.60/0.71) are larger than that in $KMgI_3$ (0.31), whereas the hole effective masses m_h^* (0.13/0.14) are much smaller than the remarkably large value of 5.96 for $KMgI_3$. These materials are anisotropic in electronic structure and thus the effective masses have different values according to the direction. For the solid solutions with $0.5 \leq x \leq 1$ with higher band gaps, the m_h^* values are much over 1, whereas the solid solutions with $0.0 \leq x \leq 0.5$ with proper band gaps for photovoltaic or photocatalytic applications have reasonable m_e^* and m_h^* values.

To get a direct understanding of their optical properties, we estimate the photoabsorption coefficients from the frequency-dependent dielectric constants, which are calculated by the DFPT method with PBE functional (see Fig. S6† for real and imaginary parts of dielectric functions). Fig. 6 shows the calculated photoabsorption coefficients as a function of photon energy for solid solutions $KB_{1-x}Mg_xI_3$ (B = Ge, Sn) with $x = 0$, 0.25, 0.5 (I, II), 0.75 and 1. It could be seen that $KGeI_3$ and $KSnI_3$ have reasonable photoabsorption coefficients for photovoltaic

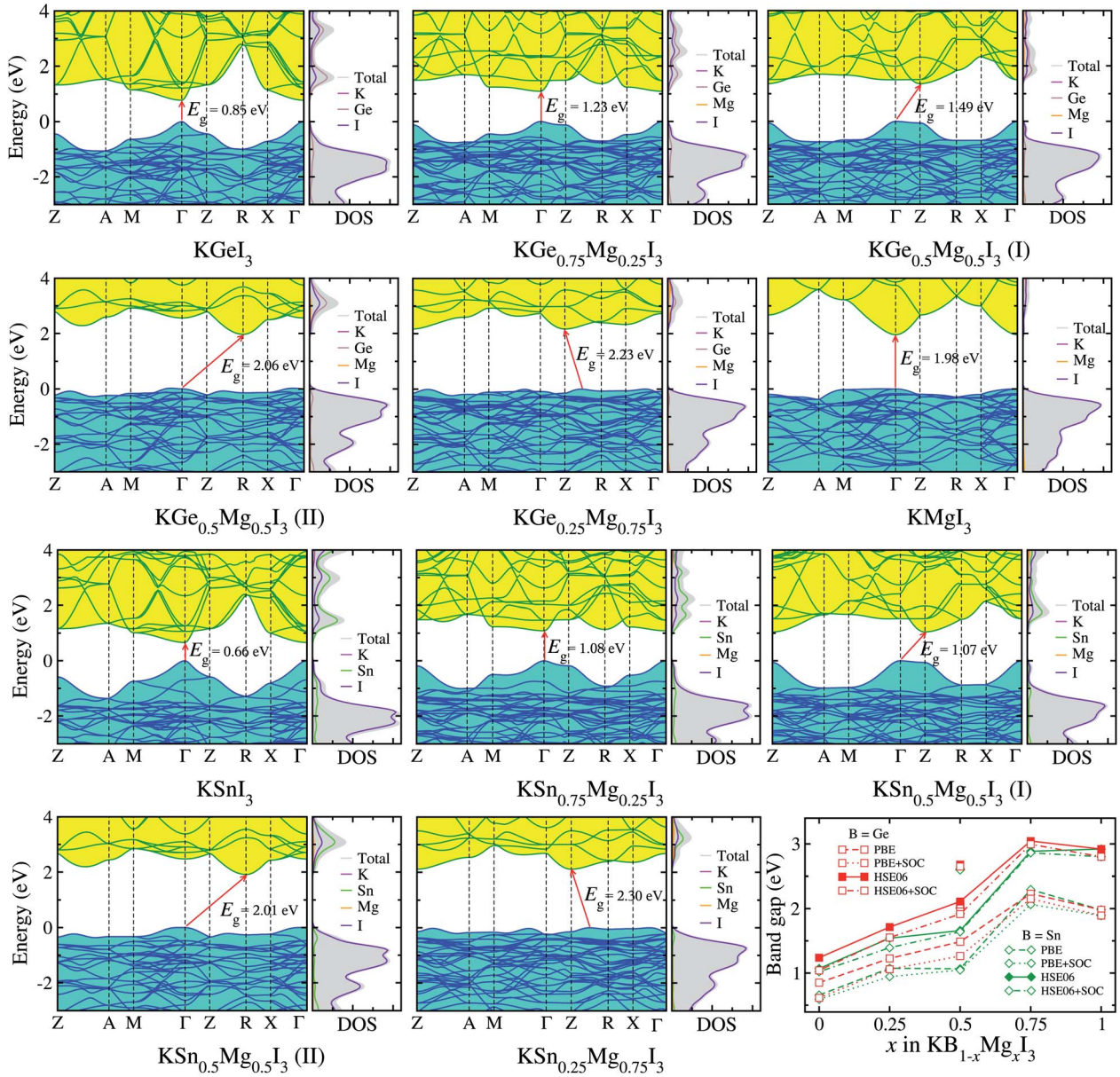

Fig. 4 Electronic band structures and partial density of states (DOS) of potassium iodide perovskite solid solutions $KB_{1-x}Mg_xI_3$ (B = Ge, Sn) calculated with PBE functional, and band gaps calculated by using PBE and HSE06 functionals with and without SOC effect, as a function of Mg content x. For $x = 0.5$ solid solutions, different configurations (I) and (II) shown in Fig. 1 are considered. The valence band maximum is set to be zero.

and photocatalytic applications with the highest peaks in the visible light region, but $KMgI_3$ is not suitable for visible light absorption. When mixing with Mg on the B-site, the first peaks look lower with the increasing Mg content. In accordance with the above analysis, the solid solutions with $x = 0.25$ and 0.5 are found to have appropriate optical properties with suitable photoabsorption coefficients to visible light.

3.3 Band edge alignment with water redox potentials

As a final step, we determine the exact band energy levels of the solid solutions with respect to the water redox potentials as well as an external vacuum level for testing photocatalytic water splitting. To estimate the absolute band energy levels, the two-equivalent slab supercells for the (001) surface with BI_2 termination, which have zero net charge for the surface, are relaxed as depicted in Fig. 7.[49,69] With the determined value of the vacuum level (V_{vac}), the absolute energy levels of the VBM and CBM are estimated following eqn (6) and (7). According to the established mechanism of photocatalytic water splitting,[77] the valence electrons are first excited from the VBM to the CBM by absorption of a photon, generating the electron–hole pairs. To proceed with water splitting, the CBM level should be more negative than the redox potential of H^+/H_2, while the VBM level should be more positive than the oxidation potential of H_2O/O_2.

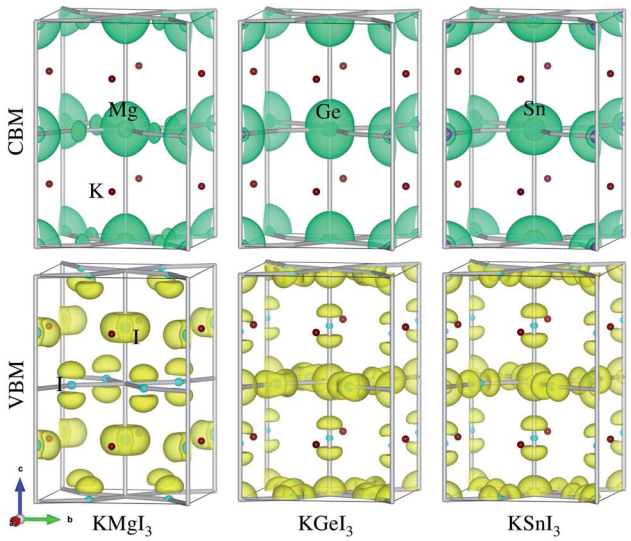

Fig. 5 Isosurface plot of electronic charge density associated with CBM and VBM for potassium iodide perovskite KBI_3 (B = Mg, Ge, Sn) in tetragonal phase, estimated at the value of 0.0017 e Å^{-3}.

Table 3 Effective masses of electron m_e^* and hole m_h^*, and reduced effective mass $1/m_r^* = 1/m_e^* + 1/m_h^*$, from the bands calculated with PBE

System	x	m_e^*	m_h^*	m_r^*
$KGe_{1-x}Mg_xI_3$	0.00	0.60	0.13	0.11
	0.25	0.67	0.22	0.17
	0.50 (I)	0.36	0.60	0.22
	0.50 (II)	0.42	3.98	0.38
	0.75	0.48	3.36	0.42
	1.00	0.31	5.96	0.30
$KSn_{1-x}Mg_xI_3$	0.00	0.71	0.14	0.11
	0.25	0.82	0.21	0.17
	0.50 (I)	0.35	0.58	0.85
	0.50 (II)	0.58	2.55	0.47
	0.75	0.90	3.13	0.71
	1.00	0.31	5.96	0.30

When meeting this condition, the electron–hole pairs migrate to the surface of the photocatalyst. At the active sites on the surface, the electrons reduce water to hydrogen as $2H^+ + 2e^- \rightarrow H_2$; E_0 *vs.* NHE = 0, while the holes oxidize water to oxygen as $2H_2O \rightarrow O_2 + 4H^+ + 4e^-$; E_0 *vs.* NHE = 1.23 V. Here, NHE means normal hydrogen electrode. Meanwhile, considering that the water splitting occurs in liquid medium, the standard water redox potentials can be changed by the pH value of the medium as follows,[78]

$$E^{red}_{H^+/H_2} = -4.44 + 0.059 \times pH \ (eV) \quad (9)$$

$$E^{ox}_{H_2O/O_2} = -5.67 + 0.059 \times pH \ (eV) \quad (10)$$

In this study, we change the pH values from 3 to 11 with an interval of 2, together with the case of pH = 0.

Fig. 8 shows the band edge alignments of $KB_{1-x}Mg_xI_3$ (B = Ge, Sn) with respect to the vacuum level and the water redox

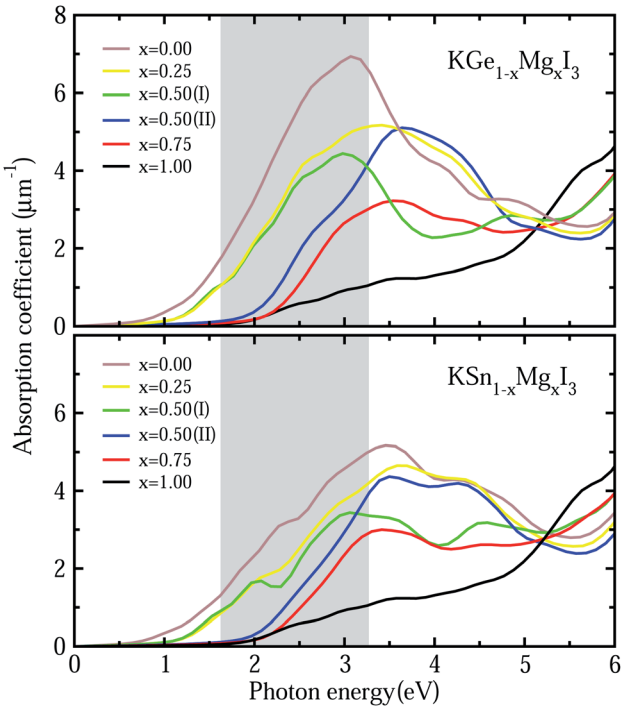

Fig. 6 Photoabsorption coefficients of $KB_{1-x}Mg_xI_3$ (B = Ge, Sn) with x = 0, 0.25, 0.5 (I, II), 0.75 and 1, calculated with PBE within density functional perturbation theory framework. Gray-colored region indicates the visible light region of 1.63–3.27 eV.

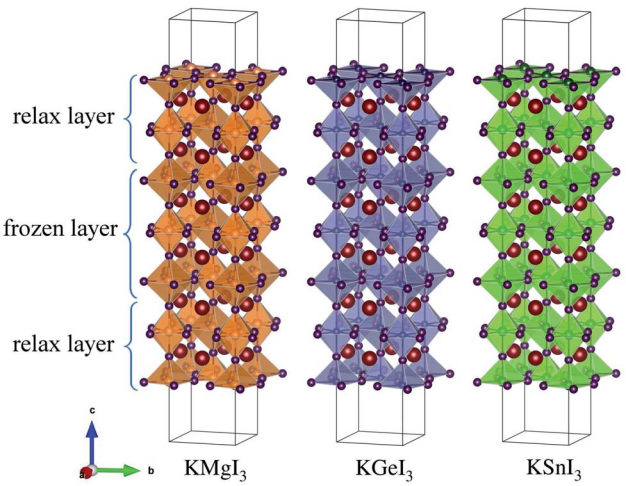

Fig. 7 Polyhedral view of surface (001) supercells with BI_2 termination of potassium iodide perovskites KBI_3 (B = Mg, Ge, Sn).

potentials, calculated by use of the hybrid HSE06 functional. When the pH = 0, the solid solutions with high Mg content $x \geq 0.5$ are shown to have the band edges straddling the water redox potentials, whereas those with lower Mg content $x < 0.5$ only have proper positions for the VBM but not for the CBM. Together with the proper band gaps of 1.66–2.11 eV, the solid solutions with $x = 0.5$ are likely to be the most promising photocatalysts for water splitting. With increasing the pH value

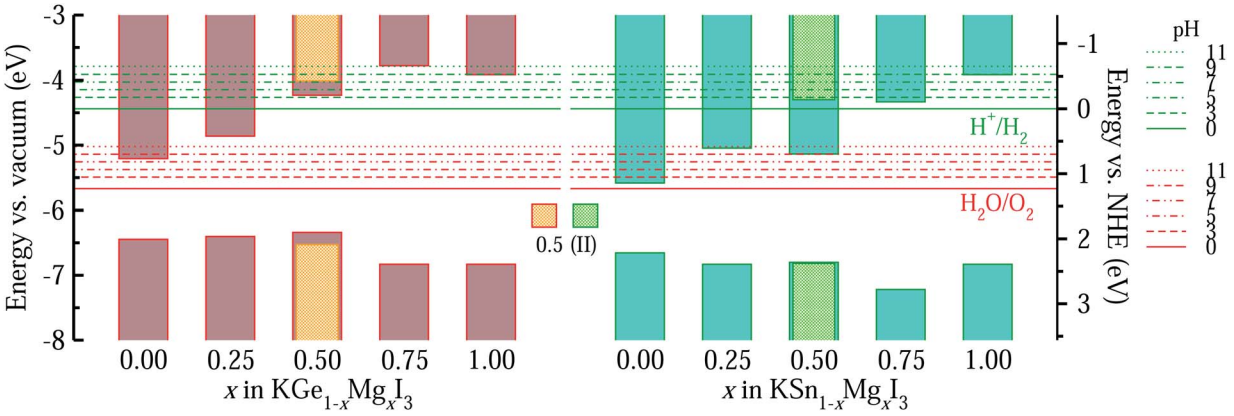

Fig. 8 Band edge alignment diagrams of $KB_{1-x}Mg_xI_3$ (B = Ge, Sn), obtained by using BI_2 terminated (001) surfaces and calculated with HSE06. All band energy levels are aligned with reference to the absolute vacuum level set as 0 eV. Hydrogen and oxygen evolution potentials from water splitting at different pH values are shown with green- and red-colored horizontal lines, respectively. NHE stands for normal hydrogen electrode. The bright green and orange bars are for solid solutions with $x = 0.5$ in the II configuration.

of the liquid medium, the water redox potential is upshifted. Then, the edges of the conduction band of the solid solutions with $x > 0.5$ become more suitable for HER, but their too wide band gaps limit the potential for utilizing as water splitting photocatalysts.

4. Conclusions

In summary, we have investigated the structural, mechanical, electronic and optical properties of potassium iodide perovskite solid solutions $KB_{1-x}Mg_xI_3$ (B = Ge, Sn) with first-principles calculations toward photocatalytic water splitting. From their Goldschmidt tolerance factors ranging from 0.81 to 0.87, these solid solutions were said to be safely crystallized to perovskite structure in the tetragonal phase, although their octahedral factors of 0.33–0.43 are somewhat smaller than the limit of 0.41. We demonstrated that the KBI_3 solid solutions with B-site cation mixing between B = Ge/Sn and Mg become thermodynamically stable by configurational entropy and meet Vegard's law well with respect to lattice constants, B–I bond length, and elastic constants. The band gaps calculated with HSE06 were found to be increased as the ionic radius of the B-site cation decreases, following the quadratic function of mixing ratio. Moreover, the solid solutions with $0.25 \leq x \leq 0.5$ were shown to have proper band gaps of 1.5–2.2 eV, reasonable effective masses, and photoabsorption coefficients suitable for absorbing sunlight. Finally, we determined the band edge alignment with respect to the water redox potentials with different pH values, revealing that $KB_{0.5}Mg_{0.5}I_3$ (B = Ge, Sn) is the most promising photocatalyst for water splitting. We believe our work highlights the potential of the lead-free potassium iodide perovskites, motivating experimentalists to synthesize them for photovoltaic or photocatalytic applications.

Conflicts of interest

There are no conflicts to declare.

Acknowledgements

This work is supported as part of the research project "Design of New Energy Materials" (No. 2021-12) by the State Commission of Science and Technology, DPR Korea. Computations have been performed on the HP Blade System C7000 (HP BL460c) managed by the Faculty of Materials Science, Kim Il Sung University.

References

1 J. Jia, L. C. Seitz, J. D. Benck, Y. Huo, Y. Chen, J. W. D. Ng, T. Bilir, J. S. Harris and T. F. Jaramillo, *Nat. Commun.*, 2016, **7**, 13237.
2 D. Wu, X. Zhang, Y. Jing, X. D. Zhao and Z. Zhou, *Nano Energy*, 2016, **28**, 390–396.
3 T. Takata, J. Jiang, Y. Sakata, M. Nakabayashi, N. Shibata, V. Nandal, K. Seki, T. Hisatomi and K. Domen, *Nature*, 2020, **581**, 411–414.
4 T. Hisatomi and K. Domen, *Nat. Catal.*, 2019, **2**, 387–399.
5 B. Ma, J. Zhao, Z. Ge, Y. Chen and Z. Yuan, *Sci. China Mater.*, 2020, **63**, 258–266.
6 Z. Zhao, B. Fu, X. Li, Z. Ge, B. Ma and Y. Chen, *ACS Appl. Energy Mater.*, 2020, **3**, 10910–10919.
7 Z. Zhao, B. Fu, X. Li, Z. Ge, B. Ma and Y. Chen, *Chem. Rev.*, 2020, **120**, 919–985.
8 B. Ma, Z. Yang, Y. Chen and Z. Yuan, *Nano Res.*, 2019, **12**, 375–380.
9 G. Liao, C. Li, X. Li and B. Fang, *Cell Rep. Phys. Sci.*, 2021, **2**, 100355.
10 Y. Liu, S. Shen, Z. Li, D. Ma, G. Xu and B. Fang, *Mater. Charact.*, 2021, **174**, 111031.
11 G. Liao, Y. Gong, L. Zhang, H. Gao, G.-J. Yang and B. Fang, *Energy Environ. Sci.*, 2019, **12**, 2080–2147.
12 G. Liao, J. Fang, Q. Li, S. Li, Z. Xu and B. Fang, *Nanoscale*, 2019, **11**, 7062–7096.
13 K. Reilly, B. Fang, F. Taghipour and D. Wilkinson, *J. Catal.*, 2017, **353**, 63–73.

14 D. Xu, Q. Chu, Z. Wu, Q. Chen, S.-Q. Fan, G.-J. Yang and B. Fang, *J. Catal.*, 2015, **325**, 118–127.
15 Y.-J. Wang, G. Chang, Q. Chen, G.-J. Yang, S.-Q. Fan and B. Fang, *Chem. Commun.*, 2015, **51**, 685–688.
16 S.-C. Yang, G. Chang, G.-J. Yang, Y.-J. Wang and B. Fang, *Catal. Sci. Technol.*, 2015, **5**, 228–233.
17 K. S. Schanze, P. V. Kamat, P. Yang and J. Bisquert, *ACS Energy Lett.*, 2020, **5**, 2602–2604.
18 S. Singh, H. Chen, S. Shahrokhi, L. P. Wang, C.-H. Lin, L. Hu, X. Guan, A. Tricoli, Z. J. Xu and T. Wu, *ACS Energy Lett.*, 2020, **5**, 1487–1497.
19 H. Huang, B. Pradhan, J. Hofkens, M. B. J. Roeffaers and J. A. Steele, *ACS Energy Lett.*, 2020, **5**, 1107–1123.
20 X. Zhu, Y. Lin, J. San Martin, Y. Sun, D. Zhu and Y. Yan, *Nat. Commun.*, 2019, **10**, 2843.
21 S. Roy and G. G. Botte, *RSC Adv.*, 2018, **8**, 5388–5394.
22 H. J. Snaith, *Nat. Mater.*, 2018, **17**, 372–376.
23 H. Baig, H. Kanda, A. M. Asiri, M. K. Nazeeruddin and T. Mallick, *Sustainable Energy Fuels*, 2020, **4**, 528.
24 C.-J. Yu, U.-G. Jong, M.-H. Ri, G.-C. Ri and Y.-H. Pae, *J. Mater. Sci.*, 2016, **51**, 9849–9854.
25 A. Kojima, K. Teshima, Y. Shirai and T. Miyasaka, *J. Am. Chem. Soc.*, 2009, **131**, 6050–6051.
26 Research Cell Efficiency Records, *National Renewable Energy Laboratory (NREL)*, 2020.
27 S. Körbel, M. A. L. Marques and S. Botti, *J. Mater. Chem. C*, 2016, **4**, 3157–3167.
28 G. Han, H. D. Hadi, A. Bruno, S. A. Kulkarni, T. M. Koh, L. H. Wong, C. Soci, N. Mathews, S. Zhang and S. G. Mhaisalkar, *J. Phys. Chem. C*, 2018, **122**, 13884–13893.
29 M. Pazoki and T. Edvinsson, *Sustainable Energy Fuels*, 2018, **2**, 1430–1445.
30 S. Park, W. J. Chang, C. W. Lee, S. Park, H. Y. Ahn and K. T. Nam, *Nat. Energy*, 2017, **2**, 16185.
31 X. Wang, H. Wang, H. Zhang, W. Yu, X. Wang, Y. Zhao, X. Zong and C. Li, *ACS Energy Lett.*, 2018, **3**, 1159–1164.
32 J. Luo, H. Yang, Z. Liu, F. Li, S. Liu, J. Ma and B. Liu, *Mater. Today Chem.*, 2019, **12**, 1–12.
33 Y. Wu, P. Wang, X. Zhu, Q. Zhang, Z. Wang, Y. Liu, G. Zou, Y. Dai, M.-H. Whangbo and B. Huang, *Adv. Mater.*, 2018, **30**, 1704342.
34 R. Li, X. Li, J. Wu, X. Lv, Y.-Z. Zheng, Z. Zhao, X. Ding, X. Tao and J.-F. Chen, *Appl. Catal., B*, 2019, **259**, 118075.
35 H. Wang, X. Wang, R. Chen, H. Zhang, X. Wang, J. Wang, J. Zhang, L. Mu, K. Wu, F. Fan, X. Zong and C. Li, *ACS Energy Lett.*, 2019, **4**, 40–47.
36 Y.-H. Kye, C.-J. Yu, U.-G. Jong, Y. Chen and A. Walsh, *J. Phys. Chem. Lett.*, 2018, **9**, 2196–2201.
37 U.-G. Jong, C.-J. Yu, G.-C. Ri, A. P. McMahon, N. M. Harrison, P. R. F. Barnes and A. Walsh, *J. Mater. Chem. A*, 2018, **6**, 1067–1074.
38 J. Yang, B. D. Siempelkamp, D. Liu and T. L. Kelly, *ACS Nano*, 2015, **9**, 1955–1963.
39 U.-G. Jong, C.-J. Yu, Y.-H. Kye, Y.-S. Kim, C.-H. Kim and S.-G. Ri, *J. Mater. Chem. A*, 2018, **6**, 17994–18002.
40 U.-G. Jong, C.-J. Yu, Y.-S. Kim, Y.-H. Kye and C.-H. Kim, *Phys. Rev. B*, 2018, **98**, 125116.
41 N. A. N. Ouedraogo, Y. Chen, Y. Y. Xiao, Q. Meng, C. B. Han, H. Yan and Y. Zhang, *Nano Energy*, 2020, **67**, 104249.
42 Y. F. Xu, M. Z. Yang, B. X. Chen, X. D. Wang, H. Y. Chen, D. B. Kuang and C. Y. Su, *J. Am. Chem. Soc.*, 2017, **139**, 5660–5663.
43 K. Chen, X. H. Deng, G. Dodekatos and H. Tüysüz, *J. Am. Chem. Soc.*, 2017, **139**, 12267–12273.
44 C.-J. Yu, U.-H. Ko, S.-G. Hwang, Y.-S. Kim, U.-G. Jong, Y.-H. Kye and C.-H. Ri, *Phys. Rev. Mater.*, 2020, **4**, 045402.
45 Z. Guan, Y. Wu, P. Wang, Q. Zhang, Z. Wang, Z. Zheng, Y. Liu, Y. Dai, M.-H. Whangbo and B. Huang, *Appl. Catal., B*, 2019, **245**, 522–527.
46 J. Li, H. Cao, W. Jiao, Q. Wang, M. Wei, I. Cantone, J. Lü and A. Abate, *Nat. Commun.*, 2020, **11**, 310.
47 C. Liu, W. Li, J. Fan and Y. Mai, *J. Energy Chem.*, 2018, **27**, 1054–1066.
48 G. Walters and E. H. Sargent, *J. Phys. Chem. Lett.*, 2018, **9**, 1018–1027.
49 Y.-K. Jung, J.-H. Lee, A. Walsh and A. Soon, *Chem. Mater.*, 2017, **29**, 3181–3188.
50 J. J. Gabriel, S. Xie, K. Choudhary, M. Sexton, S. R. Phillpot, J. Xue and R. G. Hennig, *Comput. Mater. Sci.*, 2018, **155**, 69–73.
51 L. Dimesso, C. Das, T. Mayer and W. Jaegermann, *J. Mater. Sci.*, 2018, **53**, 356–368.
52 M. R. Filip and F. Giustino, *J. Phys. Chem. C*, 2016, **120**, 166–173.
53 N. Wang, Y. Zhou, M. G. Ju, H. F. Garces, T. Ding, S. Pang, X. C. Zeng, N. P. Padture and X. W. Sun, *Adv. Energy Mater.*, 2016, **6**, 1601130.
54 T. Krishnamoorthy, H. Ding, C. Yan, W. L. Leong, T. Baikie, Z. Zhang, M. Sherburne, S. Li, M. Asta, N. Mathews and S. G. Mhaisalkar, *J. Mater. Chem. A*, 2015, **3**, 23829–23832.
55 W. Travis, E. N. K. Glover, H. Bronstein, D. O. Scanlon and R. G. Palgrave, *Chem. Sci.*, 2016, **7**, 4548–4556.
56 Z. Tang, S. Uchida, T. Bessho, T. Kinoshita, H. Wang, F. Awai, R. Jono, M. M. Maitani, J. Nakazaki, T. Kubo and H. Segawa, *Nano Energy*, 2018, **45**, 184–192.
57 M. Abdi-Jalebi, Z. Andaji-Garmaroudi, S. Cacovich, C. Stavrakas, B. Philippe, J. M. Richter, M. Alsari, E. P. Booker, E. M. Hutter, A. J. Pearson, S. Lilliu, T. J. Savenije, H. Rensmo, G. Divitini, C. Ducati, R. Friend and S. D. Stranks, *Nature*, 2018, **555**, 497–501.
58 M. Abdi-Jalebi, Z. Andaji-Garmaroudi, A. J. Pearson, G. Divitini, S. Cacovich, B. Philippe, H. Rensmo, C. Ducati, R. H. Friend and S. D. Stranks, *ACS Energy Lett.*, 2018, **3**, 2671–2678.
59 G. Kresse and J. Furthmüller, *Comput. Mater. Sci.*, 1996, **6**, 15–50.
60 J. P. Perdew, K. Burke and M. Ernzerhof, *Phys. Rev. Lett.*, 1996, **77**, 3865.
61 J. Heyd, G. E. Scuseria and M. Ernzerhof, *J. Chem. Phys.*, 2003, **118**, 8207–8215.
62 J. Heyd, G. E. Scuseria and M. Ernzerhof, *J. Chem. Phys.*, 2006, **124**, 219906.
63 F. Brivio, C. Caetano and A. Walsh, *J. Phys. Chem. Lett.*, 2016, **7**, 1083–1087.

64 C.-J. Yu, U.-S. Hwang, Y.-C. Pak, K. Rim, C. Ryu, C.-R. Mun and U.-G. Jong, *New J. Chem.*, 2020, **44**, 21218–21227.
65 G. Onida, L. Reining and A. Rubio, *Rev. Mod. Phys.*, 2002, **74**, 601–659.
66 X. Gonze, F. Jollet, F. A. Araujo, D. Adams, B. Amadon, T. Applencourt, C. Audouze, J. M. Beuken, J. Bieder, A. Bokhanchuk, *et al.*, *Comput. Phys. Commun.*, 2016, **205**, 106.
67 U.-G. Jong, C.-J. Yu, J.-S. Ri, N.-H. Kim and G.-C. Ri, *Phys. Rev. B*, 2016, **94**, 125139.
68 U.-G. Jong, C.-J. Yu, Y.-M. Jang, G.-C. Ri, S.-N. Hong and Y.-H. Pae, *J. Power Sources*, 2017, **350**, 65–72.
69 U.-G. Jong, C.-J. Yu, Y.-H. Kye, Y.-G. Choe, W. Hao and S. Li, *Inorg. Chem.*, 2019, **58**, 4134–4140.
70 V. M. Goldschmidt, *Naturwissenschaften*, 1926, **14**, 477–485.
71 M. Kar and T. Körzdörfer, *Mater. Res. Express*, 2020, **7**, 055502.
72 X. Mao, L. Sun, T. Wu, T. Chu, W. Deng and K. Han, *J. Phys. Chem. C*, 2018, **122**, 7670–7675.
73 Z. Li, M. J. Yang, J. S. Park, S.-H. Wei, J. J. Berry and K. Zhu, *Chem. Mater.*, 2016, **28**, 284–292.
74 C. Li, X. Lu, W. Ding, L. Feng, Y. Gao and Z. Guo, *Acta Crystallogr., Sect. B: Struct. Sci.*, 2008, **64**, 702–707.
75 S. F. Pugh, *Philos. Mag.*, 1954, **45**, 823–843.
76 P. Umari, E. Mosconi and F. D. Angelis, *Sci. Rep.*, 2015, **4**, 4467.
77 U. Gupta and C. N. R. Rao, *Nano Energy*, 2017, **41**, 49–65.
78 R. Meng, X. Sun, D. Yang, J. Bao and X. Chen, *Appl. Mater. Today*, 2018, **13**, 276–284.